Optics & Laser Technology 199 (2026) 115012

Contents lists available at ScienceDirect

Optics and Laser Technology

journal homepage: www.elsevier.com/locate/jolt

Full length article

Simultaneous multi-gas detection using IPDA lidar with InGaAs/InP single-photon detector

Kexin Guo[a,b,1], Haobin Han[a,b,1], Zhekai Li[a,b], Jiadong Hu[a,b,c], Jiawei Qiu[a,b], Saifen Yu[a,b,*], Zhen Zhang[a,b], Haiyun Xia[a,b,c,d]

[a] State Key Laboratory of Climate System Prediction and Risk Management, NUIST, Nanjing, 210044, China
[b] School of Atmospheric Physics, Nanjing University of Information Science and Technology, Nanjing, 210044, China
[c] Institute of Lidar Technology, GuangZai Co. Ltd., Hangzhou, 310005, China
[d] School of Earth and Space Science, University of Science and Technology of China, Hefei, 230026, China

HIGHLIGHTS

- A specific timing strategy is adopted to arrange and combine the absorption lines of multiple gases in the time domain.
- The single photon detector realizes high temporal resolution and superior detection capability for weak signals.
- The system realizes the detection of all gases within a single scanning period.
- Only the identified gases undergo detailed analysis one-by-one, improving the detection efficiency and accuracy.

ARTICLE INFO

Keywords:
Single-photon
Multi-gas
Time-domain overlapping spectroscopy
Timing strategy

ABSTRACT

A single-photon multi-gas integrated path differential absorption (IPDA) lidar system based on time-domain overlapping spectroscopy with a reconfigurable optical path is proposed and demonstrated. A specific timing strategy is adopted to arrange and combine the absorption lines of multiple gases in the time domain. Unlike the traditional time-division multiplexing technique that detects gases sequentially, this system realizes the detection of all gases within a single scanning period, using single-pixel single-photon detector. Only the identified gases undergo detailed analysis one-by-one, improving the detection efficiency and accuracy. Utilizing the high temporal resolution and superior detection capability for weak signals of the single-photon detector, the path-integrated concentrations of the identified gases are quantitatively estimated. The adoption of a multi-wavelength programmable grating filter further improves the capability of background noise suppression. In the first step, four types of gases are recognized using 10 μs scanning period with averaging time of 1 s. In the second step, continuous monitoring of the path-integrated concentrations of the C_2H_2 and CH_4 over 4 h is carried out to verify the stability and accuracy of the system. The mean and standard deviations are 0.03% and 0.43% for C_2H_2, and 0.05% and 0.48% for CH_4, respectively.

1. Introduction

Gas leakage in industrial parks, urban pipelines, and mining sites is a major source of environmental pollution and safety risks [1–3]. Gases emitted from different industrial processes, while complex in composition, contain identifiable characteristic components–such as volatile organic compounds (VOCs) from chemical plants, methane (CH_4) and carbon monoxide (CO) from coal mines [4,5]. However, the diversity of gas leakage types means that traditional single-gas monitoring solutions face challenges of low efficiency and high costs. Therefore, the development of a continuous day-and-night monitoring system capable of rapidly and accurately identifying multiple gases is essential for effective leakage early-warning and traceability management.

Spectroscopy, with its “molecular fingerprint”-level high selectivity and high sensitivity, has become a core technical support for multi-gas detection in fields such as environmental monitoring, industrial safety, and scientific research [6–8]. Depending on the detection distance and

* Corresponding author at: State Key Laboratory of Climate System Prediction and Risk Management, NUIST, Nanjing, 210044, China.
Email address: sfyu@nuist.edu.cn (S. Yu).

[1] These authors contributed equally to this work.

https://doi.org/10.1016/j.optlastec.2026.115012
Received 15 December 2025; Received in revised form 29 January 2026; Accepted 20 February 2026
Available online 24 February 2026

methodology, this technological framework is primarily divided into two categories: in-situ detection and remote sensing. Representative techniques for in-situ multi-gas detection include cavity ring-down spectroscopy [9], tunable diode laser absorption spectroscopy, photoacoustic spectroscopy [10], and optical frequency comb spectroscopy [11–13]. These techniques enable rapid response within a localized area and achieve high-precision detection. In contrast, remote sensing enables the retrieval of regional gas distribution under non-contact conditions, featuring long-detection range [14,15]. Mainstream technologies of multi-gas remote sensing include differential optical absorption spectroscopy (DOAS) [16] and Fourier transform infrared (FTIR) spectroscopy [17]. DOAS typically employs a broadband light source and a spectrometer to resolve and analyze the differential absorption features of gases, primarily in the ultraviolet (UV) and visible (Vis) spectral regions. However, its spectral resolution is generally limited to approximately 0.1 nm, which makes it suitable for detecting gases with absorption linewidths on the nanometer scale in the UV–Vis bands. FTIR technology has been widely adopted due to the advantage of broad spectral coverage in the infrared band, allowing simultaneous capture of characteristic absorption features from multiple gases [18,19]. The principle of FTIR technology is based on Fourier-transform spectroscopy, where the core lies in using an interferometer to acquire a time-domain interferogram that contains the sample absorption information. The time-domain interferogram is then converted into a frequency-domain spectrum via Fourier transform. However, this process imposes stringent requirements on instrument stability. Furthermore, FTIR commonly relies on sunlight as the light source for passive remote sensing, which poses challenges for continuous monitoring during nighttime and under complex weather conditions.

Inspired by the FTIR principle of time-domain to frequency-domain conversion, we propose a single-photon multi-gas sensing system based on time-domain overlapping spectroscopy with a reconfigurable optical path, offering high flexibility and scalability. The laser source array of the system can be reconfigured easily, depending on the gases under test (GUT). The time delays between the triggers of different lasers are designed to separate the absorption peaks of the GUT that overlap in the time domain, thereby enabling the identification of multiple gases within a single period simultaneously. Meanwhile, single-photon detector (SPD) is employed to achieve the high-sensitivity detection of extremely weak signals [20,21]. The broad response spectrum (1500–1700 nm) of the InGaAs/InP SPD covers abundant gas absorption lines, making it suitable for multi-gas detection [22]. The system enables rapid, precise and day-and-night continuous detection of multiple gases in the atmosphere, without mechanical scanning.

2. Experimental description

2.1. Optical layout and system parameters

The schematic diagram and the photograph of the lidar system are presented in Fig. 1(a) and (b), respectively. Four lasers with center wavelengths of 1531.588 nm (L-C_2H_2), 1548.190 nm (L-$H^{13}CN$), 1568.035 nm (L-CO), and 1653.725 nm (L-CH_4) are used to detect acetylene (C_2H_2), hydrogen cyanide ($H^{13}CN$), CO, and CH_4, respectively. The specific absorption lines for these gases are chosen to avoid strong water vapor interference and mutual overlap, while maintaining adequate absorption strength for reliable detection. The laser beams at different wavelengths from the four lasers are combined into one single-mode fiber (SMF) by a wavelength division multiplexer (WDM). Since C_2H_2, $H^{13}CN$, CO, and CH_4 are toxic and flammable gases, four fiber-coupled sealed gas cells are connected in series for demonstration purposes, as denoted G_1-G_4 in Fig. 1(a). The system parameters and the concentrations of each gas cell are described in Table 1.

The laser beam is collimated and expanded by the transmitter of a double-D-shaped telescope, then projected into an open path onto a non-cooperative target (a white wall located 20 m away). The backscattered light is collected by the receiver onto a multi-mode fiber (MMF), rather than an SMF. This configuration enhances the optical coupling efficiency

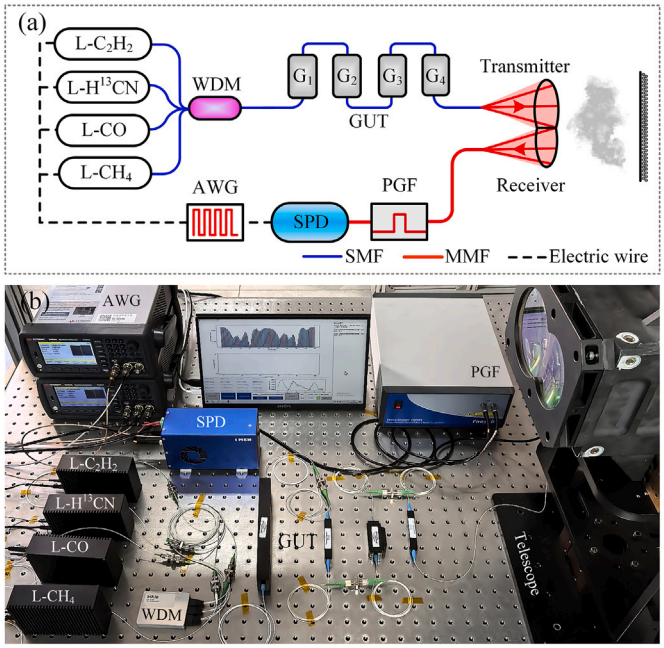

Fig. 1. Schematic diagram of the single-photon multi-gas IPDA lidar system using reconfigurable time-domain overlapping spectroscopy. (a) Schematic diagram of the system. (b) Photograph of the system.

Table 1
Key parameters of the system.

Sub-system	Parameter	Value
Laser	Wavelength (nm)	1531.588 (C_2H_2) 1548.190 ($H^{13}CN$) 1568.035 (CO) 1653.725 (CH_4)
	Linewidth (kHz)	< 200
	Scan period (μs)	10
	Maximum power (mW)	40
	Frequency scan range (GHz)	10–35
Telescope	Transmitter (mm)	90
	Receiver (mm)	70
SPD	Response range (nm)	1500–1700
	Detection efficiency (%)	15.34@1550 nm 4.87@1650 nm
	Dead time (ns)	200
	Afterpulsing probability (%)	12.76
	Dark counts (cps)	480
PGF	Operating wavelength (nm)	1526–1660
	Bandwidth (GHz)	10–5000
	Optical density (dB)	> 45
Gas cell	Concentration (ppm·m)	9500 (C_2H_2) 50,000 ($H^{13}CN$) 2,100,000 (CO) 47,000 (CH_4)

from free space to the receiver [23], and reduces the instability introduced by atmospheric turbulence [24]. A programmable grating filter (PGF) is inserted between the telescope and SPD. Four transmission windows at wavelengths of 1531.588 nm, 1548.190 nm, 1568.035 nm, and 1653.725 nm with a bandwidth of 35 GHz are used to suppress the ambient light contamination. Moreover, a broadband flat-top filter spanning from 1500 nm to 1700 nm with an out-of-band isolation of 30 dB is integrated onto the SPD, further suppressing the background light. The filtered signal is then fed into the InGaAs/InP SPD. Additionally, after each detection period of 1 s, the lasers are turned off for 0.1 s to collect the residual background noise, which can be accounted for during data processing.

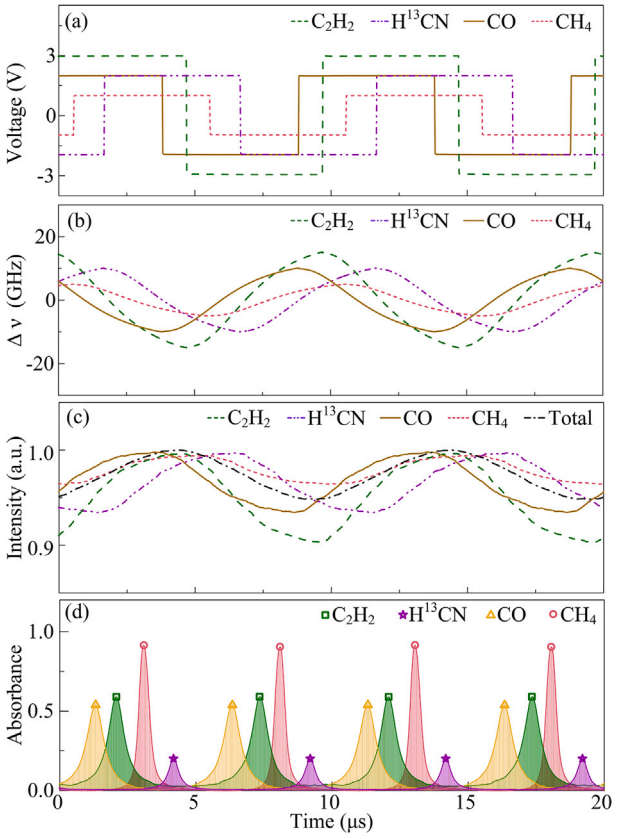

Fig. 2. (a) Asynchronous triggering sequence of the individual lasers. (b) Relative frequency variations of the lasers, where $\Delta\nu = 0$ corresponds to the center wavelength of each laser. (c) Baseline intensities of each laser and the total baseline intensity. (d) Time-domain overlapping spectra of the GUT.

2.2. Asynchronous triggering mechanism

To avoid the overlap of GUT absorption peaks and enhance gas identifiability, an asynchronous triggering mechanism is employed to arrange the absorption spectra of the four gases in the time domain. First, the center wavelength of each laser is set to the absorption peak of its corresponding target gas by adjusting the driving current. Subsequently, an arbitrary waveform generator (AWG) is used to supply 100 kHz square-wave signals with a 50% duty cycle and specific time delays to the lasers, as illustrated in Fig. 2(a). Finally, the amplitude of the modulation signal fed to each laser is adjusted depending on the linewidth of each GUT to optimize the frequency scanning range. Fig. 2(b) displays the relative frequency variation of the four lasers under asynchronous triggering signals, where $\Delta\nu = 0$ corresponds to the absorption peak of each gas. To enhance the accuracy of gas absorption peak identification and concentration retrieval, the total baseline intensity with all lasers emitting simultaneously and the individual baseline intensities from each laser are recorded to calibrate the intensity variations during the frequency scanning process, as shown in Fig. 2(c). During the calibration of the total baseline intensity and gas detection with all lasers active, the output powers of L-C_2H_2, L-$H^{13}CN$, and L-CO are set to 0.5 mW, while that of L-CH_4 is set to 1.5 mW. The power setting of CH_4 is three times higher than other gases, because the responsivity of the InGaAs/InP SPD at 1650 nm is only one third of that at 1550 nm. To enhance the signal-to-noise ratio (SNR) in individual baseline calibration and subsequent gas detection, the output powers of L-C_2H_2, L-$H^{13}CN$, and L-CO are increased to 2 mW, and that of L-CH_4 to 6 mW. Fig. 2(d) shows the temporally overlapped spectra of C_2H_2, $H^{13}CN$, CO, and CH_4. The corresponding time-domain positions of their absorption peaks within one scanning cycle (10 μs) are defined as an empirical model, as summarized in Table 2. Consequently, even in the presence of spectral overlap among the GUT, individual gases can be identified using this empirical model.

Table 2
Empirical model of absorption peaks for gases under test.

Gas type	C_2H_2	$H^{13}CN$	CO	CH_4
Up scanning (μs)	2.08	4.18	1.32	3.06
Down scanning (μs)	7.34	9.20	6.30	8.10

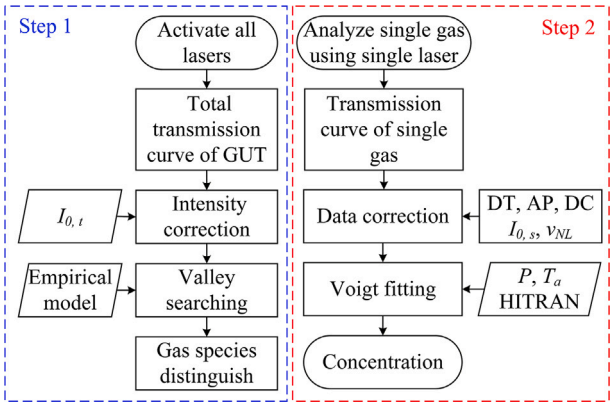

Fig. 3. Flowchart of multi-gas detection. Step 1, distinguishing gas species of the GUT. Step 2, analyzing the concentration of each single gas one by one. P, pressure, T_a, ambient temperature.

The frequency stability is very important for accurate spectrum analysis. Based on the characteristics of the employed lasers, the wavelength-current coefficient is 0.004 nm/mA and the wavelength–temperature coefficient is 0.1 nm/°C. After adopting thermal stabilization for the laser, the current stability of the driver is 0.001 mA and the temperature stability of the laser is 0.0015 °C, guaranteeing the corresponding frequency drifts of about 0.50 MHz and 18.72 MHz over 4 h, respectively. The bin width of the SPD is set to 20 ns, which corresponds to a frequency resolution of about 60 MHz. Therefore, the frequency drift induced by current and temperature fluctuations is negligible within the detection period of 1 s.

As illustrated in Fig. 3, the procedure for the multi-gas detection verification experiment can be divided into two main steps. Step 1: distinguishing gas species of the GUT. Step 2: analyzing the concentration of each single gas one by one.

3. Results and discussion

3.1. Distinguishing gas species

Step 1: First, all lasers are simultaneously activated to obtain the total transmission curve (I_t) after GUT absorption as shown in Fig. 4(a). The asymmetry in the intensity and lineshape of the gas transmission curves during up and down scanning is observed, caused by laser intensity fluctuations and nonlinear frequency variations, respectively. However, this asymmetry does not affect gas species identification, as the intensity fluctuations are normalized using the baseline intensity ($I_{0,t}$) to correct the transmission curve, as follows Qiu et al. [25]:

$$\tau(t) = I_t / I_{0,t}, \tag{1}$$

where $\tau(t)$ represents the corrected transmission curve. This correction eliminates the impact of intensity variations without requiring further data adjustments. Second, a valley-searching method using the first-order derivative is applied to the total transmission curve, as shown

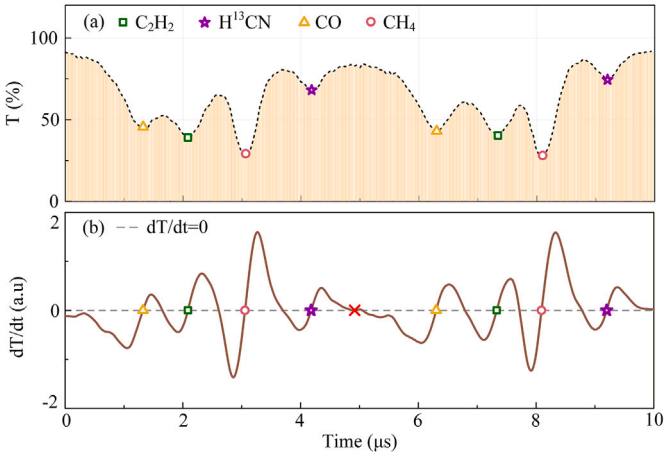

Fig. 4. Distinguishing gas species based on valley searching using first-order derivative. (a) SPD detection results with simultaneous presence of C_2H_2, $H^{13}CN$, CO, and CH_4. The yellow bars represent the raw transmission data, and the dashed line indicates the envelope of the raw transmission data. (b) Valley searching via first-order derivative. Red crosses denote outlier points not included in the empirical model. *T*, Transmission.

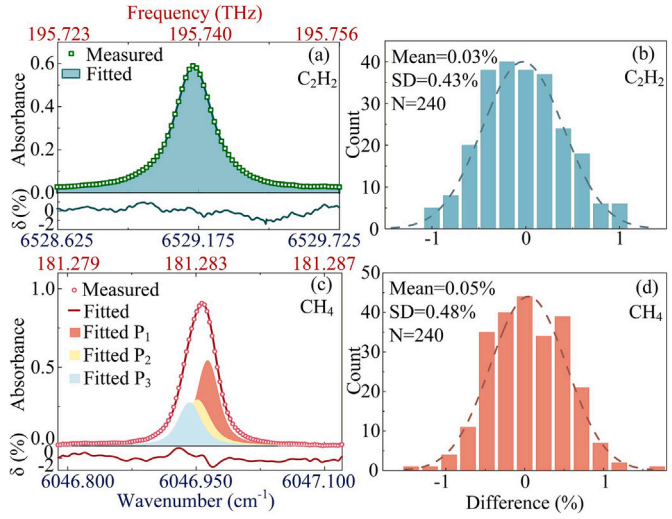

Fig. 5. (a) Voigt single-peak fitting for C_2H_2, (b) error distribution of path-integrated concentration for C_2H_2, (c) Voigt triple-peak fitting for CH_4, (d) error distribution of path-integrated concentration for CH_4. δ denotes the residual, and SD represents the standard deviation.

in Fig. 4(b), where the positions marked with different symbols correspond to the valley points. Finally, valid time-domain positions from the empirical model are incorporated to eliminate outliers. Based on the one-to-one correspondence between gases and time-domain positions defined in the empirical model, the individual gas species are successfully identified.

3.2. Gas concentration analysis

Step 2: First, to minimize inter-gas interference, only the laser corresponding to an identified gas species is activated for a detailed spectral scan. Second, the raw data of the single-gas transmission curve are sequentially corrected for intensity errors induced by the SPD's dead time (DT), afterpulsing probability (AP), dark counts (DC) and individual baseline intensities ($I_{0,s}$) [26]. The nonlinear frequency (ν_{NL}) errors induced during frequency scanning are corrected using a Mach-Zehnder interferometer combined with joint time–frequency analysis. Third, the corrected data are fitted with a Voigt profile based on the HITRAN database, and the path-integrated concentration of the identified gas is estimated using the area method. For gases with complex or overlapping spectral features, a multi-peak fitting approach is applied to separate the contributions from individual absorption lines, thereby improving the accuracy of concentration retrieval. To mitigate the impact of ambient variations on the detection, the real-time temperature and pressure data are adopted for absorption line calculation. Finally, the second step is repeated sequentially to process the remaining identified gases.

It is worth noting that the time-domain overlapping spectroscopy is different from time-division multiplexing (TDM). In TDM, lasers are activated sequentially to measure gases one by one, without crosstalk between measurements. However, the time-domain overlapping spectroscopy enables the simultaneous identification of multiple gases within a single laser scanning period, reducing the time cost. In contrast to frequency-division multiplexing (FDM), the new approach does not rely on precise spectral demultiplexing components or a detector array matched to the number of wavelengths. Instead, multi-gas discrimination is achieved through time-domain encoding of absorption lines, significantly simplifying the system configuration.

In this experiment, C_2H_2 and CH_4 are individually subjected to fine analysis, as illustrated in Fig. 5. To further evaluate system stability, path-integrated concentration sampling is performed with a time resolution of 1 s at 1-minute intervals over a continuous 4-hour monitoring period. The detailed procedures for correcting single-photon counting errors and nonlinear frequency effects in the raw data of single-gas measurements have been described in detail elsewhere [27,28]. Fig. 5(a) shows the corrected absorbance curve of C_2H_2 and the corresponding single-peak Voigt fitting result. The standard deviation of the fitting residuals is 0.49%, demonstrating excellent agreement between the experimental data and the fitted curve. Fig. 5(b) shows the statistical results of the path-integrated concentration variations for C_2H_2, with the 240 test results yielding a mean deviation of 0.03% and a standard deviation of 0.43%. Fig. 5(c) presents the corrected absorbance curve of CH_4 and its corresponding fitting result. Due to the complex absorption structure of CH_4 around 1653.725 nm, which consists of three absorption lines, a triple-peak Voigt fitting function is employed to improve accuracy, yielding a standard deviation of the fitting residuals of 0.56%. Fig. 5(d) displays the distribution histogram of CH_4 concentration measured during the 4-hour continuous monitoring period, showing a mean deviation of 0.05% and a standard deviation of 0.48%. The small mean and standard deviations observed for both gases demonstrate the high accuracy and stability of the experimental system.

To verify the system's detection performance for gases at different concentrations. C_2H_2 is pumped into a sealed gas cell with optical windows at two ends. At each gas concentration, the laser power is adjusted to achieve two light intensity levels corresponding to photon count rates of 5.2 Mcps and 520 kcps. In a single-photon detection system, the photon number determines the SNR under the assumption of Poisson noise distribution [29], and the optical depth governs the detection sensitivity. The test results are shown in Fig. 6. The standard deviation ranges from 20 to 30 ppm·m at a counting rate of 5.2 Mcps. In comparison, when the photon count rate is reduced by an order of magnitude, the standard deviation across different gas concentrations increases to about 68 to 90 ppm·m. Meanwhile, with the increase in gas concentration (i.e., the rise in absorption depth), the concentration errors under the two SNR conditions both exhibit a trend of first decreasing and then increasing. This phenomenon can be attributed to two aspects. On the one hand, the increase in absorption depth improves the sensitivity of gas detection, thus enhancing the measurement accuracy. On the other hand, an excessively large absorption depth leads to a sharp drop in the photon count over the absorption line, which in turn degrades the SNR.

Due to the limitation of the maximum counting rate of SPD, for gas species identification within a fixed detection period, the effective photon count for a single gas will decrease (leading to low SNR), as the number of target gases increases. Therefore, to increase the number of

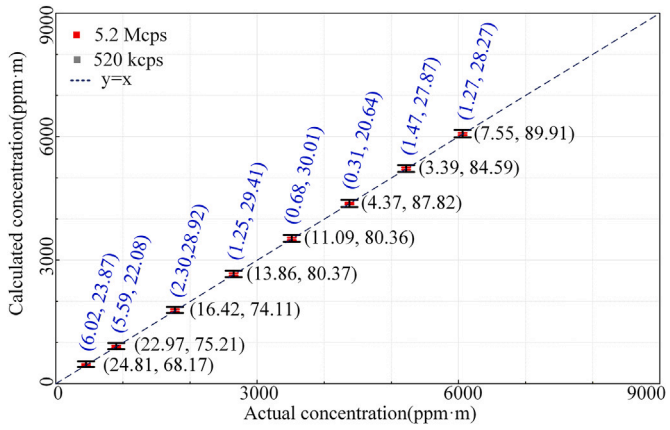

Fig. 6. The path-integrated concentration error analysis of C_2H_2 at the photon counting rate of 5.2 Mcps and 520 kcps. Data shown in the format of (mean error, standard deviation).

detectable gases while ensuring sufficient SNR, the scanning period must be extended accordingly. In applications involving a large number of gases, these trade-offs need to be considered. In specific scenarios where the gas species are known a priori, such as coal mines and chemical plants, the system can be configured by selecting lasers corresponding to the target gases, which improves both the identification efficiency and the detection accuracy of the system.

4. Conclusion

In summary, a single-photon IPDA lidar system based on time-domain overlapping spectroscopy with a reconfigurable optical path is proposed and experimentally demonstrated. By arranging gas absorption peaks in temporal sequences, all target gases can be detected simultaneously within a single scanning period, enabling rapid identification of leaking gas species. Moreover, performing fine analysis exclusively on the identified gases enhances the accuracy of concentration detection. The effects of real atmospheric conditions (e.g., atmospheric turbulence, aerosol scattering, and other factors) are considered in the experimental system design.

CRediT authorship contribution statement

Kexin Guo: Writing – original draft, Visualization, Validation, Software, Formal analysis, Data curation. **Haobin Han:** Writing – original draft, Validation, Formal analysis, Data curation. **Zhekai Li:** Writing – review & editing, Investigation. **Jiadong Hu:** Writing – review & editing, Software, Methodology. **Jiawei Qiu:** Writing – review & editing, Project administration, Conceptualization. **Saifen Yu:** Writing – review & editing, Writing – original draft, Validation, Supervision, Funding acquisition. **Zhen Zhang:** Writing – review & editing, Visualization, Supervision, Investigation, Funding acquisition. **Haiyun Xia:** Writing – review & editing, Resources, Project administration, Methodology, Funding acquisition, Conceptualization.

Funding

This work is supported by the National Natural Science Foundation of China (No. 42305147), the National Natural Science Foundation of China (No. 42405138), and the Natural Science Foundation of Jiangsu Province (No. BK20230428).

Declaration of competing interest

The authors declare that they have no known competing financial interests or personal relationships that could have appeared to influence the work reported in this paper.

Data availability

Data underlying the results presented in this paper are not publicly available at this time but may be obtained from the authors upon reasonable request.

References

[1] S.I. Kondratyev, D. Baskanbayeva, K. Yelemessov, E.V. Khekert, V.E. Privalov, Y. Sarsenbayev, V.A. Turkin, Control of hydrogen leaks from storage tanks and fuel supply systems to mining transport infrastructure facilities, Int. J. Hydrog. Energy 95 (2024) 212–216, https://doi.org/10.1016/j.ijhydene.2024.11.182.

[2] C. Zhang, T. Xu, G. Wu, F. Gao, Y. Liu, D. Gong, H. Wang, C. Zhang, B. Wang, Reduction of fugitive VOC emissions using leak detection and repair (LDAR) in a petroleum refinery of Pearl River Delta, China, Appl. Energy. 324 (2022) 119701, https://doi.org/10.1016/j.apenergy.2022.119701

[3] Z. Pei, G. Han, H. Mao, C. Chen, T. Shi, K. Yang, X. Ma, W. Gong, Improving quantification of methane point source emissions from imaging spectroscopy, Remote Sens. Environ. 295 (2023) 113652, https://doi.org/10.1016/j.rse.2023.113652

[4] H. Wang, S. Sun, L. Nie, Z. Zhang, W. Li, Z. Hao, A review of whole-process control of industrial volatile organic compounds in China, J. Environ. Sci. 123 (2023) 127–139, https://doi.org/10.1016/j.jes.2022.02.037

[5] M. Menoud, C. van der Veen, J. Necki, J. Bartyzel, B. Szénási, M. Stanisavljević, I. Pison, P. Bousquet, T. Röckmann, Methane (CH_4) sources in Krakow, Poland: insights from isotope analysis, Atmos. Chem. Phys. 21 (17) (2021) 13167–13185, https://doi.org/10.5194/acp-21-13167-2021

[6] S. Yu, Z. Zhang, H. Xia, X. Dou, T. Wu, Y. Hu, M. Li, M. Shangguan, T. Wei, L. Zhao, Photon-counting distributed free-space spectroscopy, Light: Sci. Appl. 10 (1) (2021) 212, https://doi.org/10.1038/s41377-021-00650-2

[7] J. Sun, J. Chang, C. Wang, J. Shao, Tunable diode laser absorption spectroscopy for detection of multi-component gas: a review, Appl. Spectrosc. Rev. 59 (8) (2024) 1086–1107, https://doi.org/10.1080/05704928.2024.2302608

[8] Y. Wang, L. Wan, Z. Song, L. Xu, J. Liu, H. Xu, Robust gas quantification in mid-infrared FTIR spectroscopy via a suppression-adaptation-optimization model, Opt. Express 33 (17) (2025) 35865–35880, https://doi.org/10.1364/OE.569370

[9] C. Lin, R. Hu, P. Xie, S. Lou, G. Zhang, J. Tong, J. Liu, W. Liu, Nocturnal atmospheric chemistry of NO_3 and N_2O_5 over Changzhou in the Yangtze River Delta in China, J. Environ. Sci. 114 (2022) 376–390, https://doi.org/10.1016/j.jes.2021.09.016

[10] M. Li, T. Zhu, G. Wu, Y. Guan, Z. Gong, W. Peng, L. Mei, A double dual-resonance enhanced photoacoustic spectroscopy gas sensor for simultaneous C_2H_2 and CH_4 detection, Sens. Actuators B: Chem. 445 (2025) 138617, https://doi.org/10.1016/j.snb.2025.138617

[11] Z. Zhang, H. Xia, S. Yu, L. Zhao, T. Wei, M. Li, Femtosecond imbalanced time-stretch spectroscopy for ultrafast gas detection, Appl. Phys. Lett. 116 (17) (2020) 171106, https://doi.org/10.1063/1.5143790

[12] N. Picqué, T.W. Hänsch, Frequency comb spectroscopy, Nat. Photonics 13 (3) (2019) 146–157, https://doi.org/10.1038/s41566-018-0347-5

[13] I. Coddington, N. Newbury, W. Swann, Dual-comb spectroscopy, Optica 3 (4) (2016) 414–426, https://doi.org/10.1364/OPTICA.3.000414

[14] S. Yu, K. Guo, S. Li, H. Han, Z. Zhang, H. Xia, Three-dimensional detection of CO_2 and wind using a 1.57-μm coherent differential absorption LIDAR, Opt. Express 32 (12) (2024) 21134–21148, https://doi.org/10.1364/OE.523904

[15] A.K. Thorpe, P.E. Dennison, L. Guanter, C. Frankenberg, I. Aben, Special issue on remote sensing of greenhouse gas emissions, Remote Sens. Environ. 277 (2022) 113069, https://doi.org/10.1016/j.rse.2022.113069

[16] C. Xing, S. Xu, Y. Song, C. Liu, Y. Liu, K. Lu, W. Tan, C. Zhang, Q. Hu, S. Wang, H. Wu, H. Lin, A new insight into vertical differences in NO_2 heterogeneous reaction to produce HONO over inland and marginal seas, Atmos. Chem. Phys. 23 (10) (2023) 5815–5834, https://doi.org/10.5194/acp-23-5815-2023

[17] T. Xu, L. Xu, Y. Sun, W. Liu, J. Liu, Robust identification of gas mixtures from FTIR spectra using attention mechanism to mitigate instrument line shape variations, Anal. Chem. 97 (42) (2025) 23312–23320, https://doi.org/10.1021/acs.analchem.5c03975

[18] C. Shan, W. Wang, C. Liu, Y. Guo, Y. Xie, Y. Sun, Q. Hu, H. Zhang, H. Yin, N. Jones, Retrieval of vertical profiles and tropospheric CO_2 columns based on high-resolution FTIR over Hefei, China, Opt. Express 29 (4) (2021) 4958–4977, https://doi.org/10.1364/OE.411383

[19] M. Zhou, Q. Ni, Z. Cai, B. Langerock, J. Jiang, K. Che, J. Wang, W. Nan, Y. Liu, P. Wang, Ground-based atmospheric CO_2, CH_4, and CO column measurements at golmud in the Qinghai-Tibetan plateau and comparisons with TROPOMI/S5P satellite observations, Adv. Atmos. Sci. 40 (2) (2023) 223–234, https://doi.org/10.1007/s00376-022-2116-0

[20] J. Titchener, D. Millington-Smith, C. Goldsack, G. Harrison, A. Dunning, X. Ai, M. Reed, Single photon lidar gas imagers for practical and widespread continuous methane monitoring, Appl. Energy. 306 (2022) 118086, https://doi.org/10.1016/j.apenergy.2021.118086

[21] M. Shangguan, Z. Yang, Z. Lin, Z. Weng, J. Sun, Full-day profiling of a beam attenuation coefficient using a single-photon underwater lidar with a large dynamic measurement range, Opt. Lett. 49 (3) (2024) 626–629, https://doi.org/10.1364/OL.514622

[22] P. Jiang, H. Xia, J. Hu, T. Wei, Estimation of atmospheric refractive index structure constant using an InGaAs/InP single-photon detector, Opt. Lett. 48 (23) (2023) 6104–6107, https://doi.org/10.1364/OL.505631

[23] C. Yu, J. Qiu, H. Xia, X. Dou, J. Zhang, J.-W. Pan, Compact and lightweight 1.5 μm lidar with a multi-mode fiber coupling free-running InGaAs/InP single-photon detector, Rev. Sci. Instrum. 89 (2018) 103106, https://doi.org/10.1063/1.5047472

[24] P. Jiang, J. Yuan, K. Wu, L. Wang, H. Xia, Turbulence detection in the atmospheric boundary layer using coherent doppler wind lidar and microwave radiometer, Remote Sens. 14 (12) (2022) 2951, https://doi.org/10.3390/rs14122951

[25] X. Qiu, X. Xiong, L. Li, G. Guo, T. Gong, S. Guo, Z. Shang, X. Sun, Y. Tian, G. Xie, H. Tan, C. Fittshen, B. Fiser, M. Szöri, G. Tarczay, C.L. Li, Development of an FDM-TDLAS sensor for long-term online monitoring of H_2S and CO to predict water wall corrosion trends, Anal. Chem. 97 (26) (2025) 14058–14066, https://doi.org/10.1021/acs.analchem.5c02691

[26] C. Yu, M. Shangguan, H. Xia, J. Zhang, X. Dou, J.-W. Pan, Fully integrated free-running InGaAs/InP single-photon detector for accurate lidar applications, Opt. Express 25 (13) (2017) 14611–14620, https://doi.org/10.1364/OE.25.014611

[27] H. Han, K. Wu, K. Guo, J. Hu, J. Qiu, S. Yu, Z. Zhang, T. Wu, H. Xia, All-fiber IPDA lidar for CH_4 leakage monitoring using InGaAs/InP single-photon detector, Opt. Express 32 (21) (2024) 37155–37166, https://doi.org/10.1364/OE.538441

[28] H. Han, K. Guo, L. Yi, Z. Li, J. Hu, S. Yu, Z. Zhang, T. Wu, J. Qiu, H. Xia, Remote sensing of flammable and toxic gases via IPDA lidar with InGaAs/InP single-photon detector over C + L band, Opt. Express 33 (18) (2025) 38828–38840, https://doi.org/10.1364/OE.572795

[29] H. Xia, C. Zhang, H. Mu, D. Sun, Edge technique for direct detection of strain and temperature based on optical time domain reflectometry, Appl. Opt. 48 (2) (2009) 189–197, https://doi.org/10.1364/AO.48.000189